A synchrotron study of defect and strain inhomogeneity in laser-assisted three-dimensionally-printed Ni-based superalloy

Yao Li,[1,2] Dan Qian,[2] Jiawei Xue,[2] Jingchun Wan,[2] Anfeng Zhang,[3,a)] Nobumichi Tamura,[4] Zhongxiao Song,[2,a)] and Kai Chen[1,2,a)]
[1]*Center for Advancing Materials Performance from the Nanoscale (CAMP-Nano), State Key Laboratory for Mechanical Behavior of Materials, Xi'an Jiaotong University, Xi'an, Shaanxi 710049, People's Republic of China*
[2]*State Key Laboratory for Mechanical Behavior of Materials, Xi'an Jiaotong University, Xi'an, Shaanxi 710049, People's Republic of China*
[3]*State Key Laboratory for Manufacturing Systems Engineering, Xi'an Jiaotong University, Xi'an, Shaanxi 710049, People's Republic of China*
[4]*Advanced Light Source, Lawrence Berkeley National Laboratory, Berkeley, California 94720, USA*

(Received 30 June 2015; accepted 18 October 2015; published online 2 November 2015)

Synchrotron X-ray microdiffraction was employed to investigate the inhomogeneous distribution of defect and residual strain in the transitional region between the dendritic and stray grains in a laser-assisted 3D printed Ni-based superalloy. The dendritic region was found to be under tensile strain transversely to the primary dendrite arm directions. The dendrite edges, where high level of strains and geometrically necessary dislocations were detected, were discerned as low angle grain boundaries. High angle grain boundaries were observed in the stray grain region, and the orientation of the strain tensor in this region varied dramatically at the micron scale, in contrast with the more or less homogeneous distribution in the dendritic region. © *2015 AIP Publishing LLC*.
[http://dx.doi.org/10.1063/1.4934839]

Serving as the core components of aeronautical and stationary gas turbines used in harsh environment, single crystal Ni-based superalloy blades are the tools of choice due to their combinatory performances, which include high temperature strength, good thermal anti-oxidation property, and excellent creep resistance.[1] To prolong the service lifetime and reduce the overall cost, development of new restoration approaches to repair the cracked or worn parts of the blades is needed, and laser additive forming, better known as laser-assisted 3D printing, is considered as one of the most promising methods.[2] In this process, the superalloy powders are continuously injected into the molten pool formed by a high-intensity scanning laser beam. Once the laser beam moves to the next scanning position, the melt nucleates and grows in epitaxy with the single crystal substrate. However, if for some reasons the nucleation density and solidification velocity exceed a critical value, numerous crystal grains will grow simultaneously with random orientations, known as "stray grains".[3] The stray grains are deleterious to the blade's resistance to creep and thermal fatigue because of the presence of high angle grain boundaries (HAGBs).[4]

It has been reported that an intrinsic strain field is generated in the conventional cast Ni-based superalloy crystal during the rapid cooling procedure. From previous modeling work, tensile strain exists in all three directions in the cast Ni-based superalloy, which is harmful for the mechanical behaviors.[7] Moreover, lattice misfit of γ/γ' phases results from the different site substitutions of refractory elements, such as Ta, W, Mo in the two phases,[5,6] and discrepancy of the relative γ/γ' volume fraction is frequently detected between the dendrite core and the interdendritic region,[7] giving rise to inhomogeneous thermal contraction and strain/stress distribution, and eventually favoring the disastrous nucleation of thermal fatigue cracks.[8] However, because of the high solidification velocity and thermal gradient, the dendritic area in 3D-printed superalloy are usually finer than in the traditionally solidified alloys; therefore, it is not trivial to investigate the defect and strain distribution at the sub-dendrite scale via the traditional characterization techniques which are limited by spatial or angular resolution.[4] In this letter, we evaluate the microstrain and defect distribution near the interface of the columnar dendrites and stray grains in a 3D-printed Ni-based superalloy using synchrotron X-ray microdiffraction (μXRD). Prominent defect inhomogeneity and strain gradient were measured at the dendrite edges.

The 3D printed DZ125L superalloy, designed in China, was deposited by an independently developed XJTU-I 3D printing system equipped with a Nd:YAG laser with a beam size of 0.5 mm. The substrate was cut from a single crystalline DZ125L superalloy cast ingot. Its surface was parallel to {001} plane, and the cross-section planes were {110} planes. The powder with grain diameters ranging from 50 to 100 μm with similar composition was coaxially injected at a 9 mm^3/s feeding speed by Ar gas carrier into the molten pool formed by the laser beam with a power of 230 W and 4 mm/s laser scanning speed. Therefore, the molten powder solidified on top of the crystal and deposited layer by layer. Table I lists the chemical compositions of the powder and substrate. More details about the 3D printer and the forming process can be found elsewhere.[9] Figure 1(a) shows schematically the epitaxial deposition of columnar dendrites on a single crystalline substrate and then the transition to equiaxed stray grains.

a)Authors to whom correspondence should be addressed. Electronic addresses: zhangaf@mail.xjtu.edu.cn; zhongxiaosong@mail.xjtu.edu.cn; and kchenlbl@gmail.com.

TABLE I. Composition of DZ125L superalloy (wt. %).

Material	Co	Cr	W	Al	Ta	Ti	Mo	C	B	Ni
Substrate	9.54	8.74	6.46	5.03	3.96	3.18	2.21	0.12	0.0076	Balance
Powder	9.64	9.70	7.14	4.90	3.78	3.12	2.18	0.09	0.015	Balance

The μXRD experiment was carried out on Beamline 12.3.2 at the Advanced Light Source (ALS) in Lawrence Berkeley National Laboratory (LBNL).[10] The sample was mounted on an **X**–**Y** scanning stage at a 45° tilt angle relative to the incident X-ray beam which has an energy bandpass of 5–24 keV, and the deposition direction was roughly parallel to the **Y**-scanning direction. A $150 \times 300\ \mu m^2$ transition region from the columnar/cellular dendrites to stray grains was scanned with the micro-focused X-ray beam using a 2 μm step size and a Laue pattern was obtained at each step using a 1 s exposure time from an area detector (DECTRIS Pilatus 1 M) placed about 140 mm away from the X-ray focal point at 90° with respect to the incoming beam. A total number of 11 250 patterns were automatically analyzed by the custom-made software XMAS[11] to obtain the crystal orientation and lattice strain at each scanning position. This technique provides high crystal orientation ($\sim 0.01°$)[12] and good deviatoric strain resolution ($\sim 10^{-4}$),[13] and the defect type and density distribution in the scan area can also be revealed from the shape of the diffraction peaks.[14,15] In all the microstructure maps and optical figures in this letter, the crystal is oriented in the same way.

After the μXRD experiment, the same sample was etched using fresh nitro-hydrochloric acid for about 5 s for metallographic observation under an optical microscope. Figures 1(b) and 1(c) show the typical hierarchical morphology of deposit microstructures of the specimen close to the area that was studied via μXRD. In Figure 1(b) with lower magnification, the substrate, columnar dendrites close to **Y** direction, and stray grains are clearly observed from bottom to top. The rectangular area is magnified and shown in Figure 1(c), in which the cellular grains are found between two adjacent layers of columnar dendrites, probably due to the thermal effects when the upper layer was deposited on the lower one. The average trunk spacing between the primary dendrites is about 12 μm, which is much smaller than the one in conventional solidification process because of the high solidification velocity and thermal gradient.[4] Moreover, the inverse pole figure (IPF) map along the **Y**-axis obtained from the μXRD measurements is shown in Figure 1(d) and proves that the growth direction of primary dendrites is almost collinear with the ⟨001⟩ direction. This is also confirmed by the poles (marked in red) of the dendritic region in the {001} stereographic projection of Figure 1(f), indicating epitaxial growth and single crystallinity. Similarly, the IPF map along the **X**-axis in Figure 1(e) and {110} stereographic projection in Figure 1(g) illustrate that the **X**-axis practically consists of the ⟨110⟩ direction in the dendritic region. Furthermore, the random scattering of the superjacent stray grain poles (in blue) in both Figures 1(f) and 1(g) indicates the absence of texture, which is attributed to numerous random nucleation sites at the front of dendrites. It is worth noting that some spurious grain boundaries displayed in the dendritic region come from failed indexation of Laue patterns due to the presence of impurities.

To emphasize the fine orientation differences in dendritic region, the disorientation angle between each pair of adjacent scan positions is calculated and plotted in Figure 2 following a method introduced in detail elsewhere.[16] The high angle (>5°) grain boundaries in the stray grain region are delineated in thick black lines, while the low angle (<5°) grain boundaries (LAGBs) are in gradient of light to dark red. Comparing with Figure 1(c), we conclude that the primary dendrite edges were LAGBs and that growth deviation occurs between each pair of adjacent primary dendrites. This observation agrees with the theoretical prediction of the extreme difficulty to obtain a perfect single crystal from solidification.[4] Dendrite growth slight deflection from its ⟨001⟩ direction is linked to solidification kinetics, including thermomechanical stresses induced by γ' participation[17] and surface tension by Marangoni convection.[4] As a consequence, the dendritic region shows a minor disorientation and LAGBs spanning over a few degrees. It should be emphasized here that only the combination of sub-degree orientation resolution and micron-scale intragranular spatial resolution offered by μXRD allows the discernment of dendrite edges for such 3D printed Ni-based superalloy specimens. As a comparison, a $150 \times 300\ \mu m^2$ area in the substrate was scanned in the similar way with 5 μm step size, and disorientation distributes in the range of $(0.05 \pm 0.03)°$, which was about one order of magnitude lower than the one in the dendritic region. The

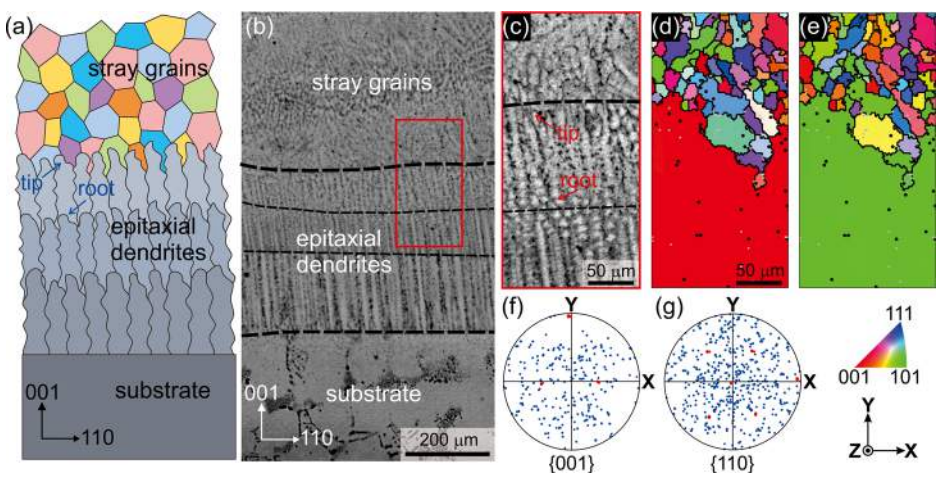

FIG. 1. (a) Schematic and (b) optical microscopic image of the laser-assisted 3D printed Ni-based superalloy deposited on the single crystalline substrate. (c) Magnified image of the dendritic and stray grains of the region indicated by the red rectangle in (b), and (d) and (e) the IPF maps along **Y**- and **X**-axis, respectively, obtained from μXRD. The {001} and {110} stereographic projection maps in (f) and (g) confirm the single crystalline nature of dendritic grains (red poles) and non-preferred orientation of stray grains (blue poles).

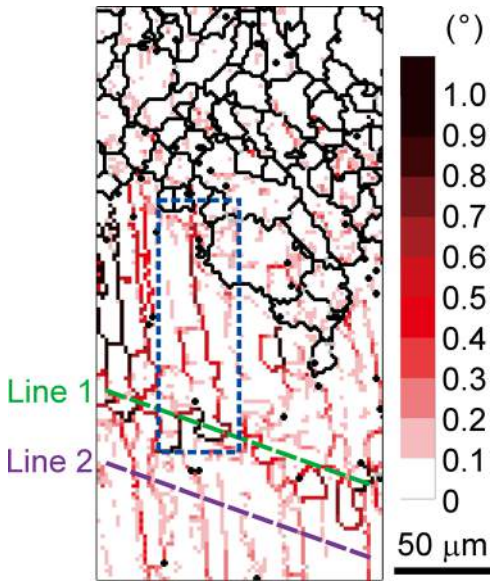

FIG. 2. Grain boundary distribution map in the μXRD studied region, in which the low angle grain boundaries in the dendritic region are delineated in the gradient of light to dark red, while the high angle boundaries (>5°) are plotted in black.

disorientation distribution statistics of both the substrate and the dendritic region are shown in Figure S1 of the supplementary material.[18]

Generally speaking, splitting and streaking of Laue diffraction peaks can be linked to the density of geometrically necessary dislocations (GNDs). From Cahn-Nye relationship,[19] in our case a disorientation gradient of 1 °/μm corresponds to a GND density of $\sim 7 \times 10^9\,\mathrm{cm}^{-2}$. To evaluate the GND distribution in local interdendritic regions, a single dendrite displayed in Figure 3(a) is considered from the highlighted rectangular region in Figure 2. The dendrite grew with about a 10° inclination from the **Y**-axis. In order to study the defect types, the diffraction peak shape evolution along three lines parallel to the dendrite axis is investigated, including two lines near both sides of dendrite edge in purple and blue, and one line at the dendrite core in orange, respectively (shown in Figure 3(b)). For simplicity, six typical 133 peaks are picked out along each line. It can be seen that the peak position is changing, indicating a rotation of the dendrite arm. Besides, the peaks are streaking or splitting near the dendrite edges, while remaining sharp in the dendrite core, indicating an inhomogeneous distribution of GNDs within a single dendrite. When comparing the crystal orientation at each scanning position along two lines (purple and green) shown in Figure 2 with the first pixel of each line, it is found that the rotation axis varies from dendrite to dendrite, as shown in Figure S2 in the supplementary material.[18] This indicates that different slip systems are activated in different dendrites. The GNDs are more prone to aggregate near the LAGBs (dendrite edges) than in the core of dendrites, and the rotation axis at the dendritic boundaries is almost randomly oriented. These are probably due to the complex flux convection in the interdendritic region.

We notice in Figure 3(b) that the peak splitting/streaking is more severe at the dendrite root than in the middle and tip. For a more general view, the 220 peak shape in all the

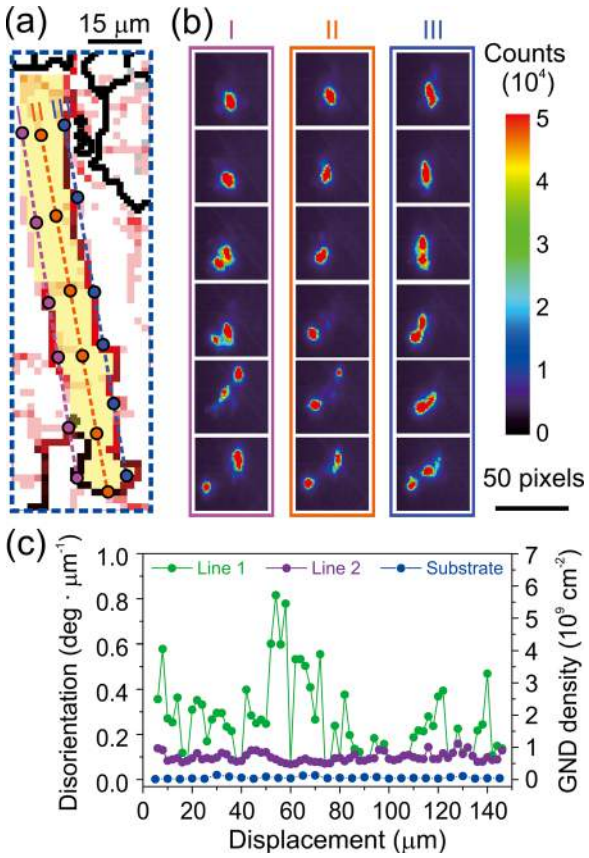

FIG. 3. (a) A magnified individual dendrite extracted from the rectangular region highlighted in Figure 2 and (b) typical 133 Laue peaks along 3 lines parallel with the dendrite growth direction marked in (a), and (c) the distribution of disorientation gradient and GND density along two lines parallel with the dendrite layer interface marked in Figure 2. The GND density of the substrate is also shown as a comparison.

patterns recorded along two lines parallel to the interface between two layers of dendrite arrays was investigated. We found that all of the peaks in the middle (purple line in Figure 2) of the dendrite layer are sharp, while the ones near the dendrite root (indicated by the green line in Figure 2) are almost all streaking or splitting. The distributions of disorientation and calculated GND density are shown in Figure 3(c) by considering both the width and splitting angle of the Laue peaks in an individual pattern, which records the GND density mainly in the depth direction (the high energy X-ray penetrates Ni by up to 40 μm while the beam size is about $1 \times 1\ \mu\mathrm{m}^2$), and the disorientation angle between two adjacent patterns, which demonstrates mainly the GND density in the **XY**-plane. From Figure 3(c), two observations can be made. First, the GND density in the investigated region of the 3D-printed superalloy is more than one order of magnitude higher than that in a material fabricated via traditional solidification process, due to the higher solidification kinetics.[20] Second, the GND density near the root of the dendrite layer is significantly higher than that in the middle. Possible explanations include that a single dendrite can be regarded as a cantilever beam anchored at the position of the solidus isotherm by the interdendritic solid,[21] and that when the new layer was deposited, the surface was not a perfect single crystal and inhomogeneous nucleation happened.[22] The beam sustained bending moments and torques on

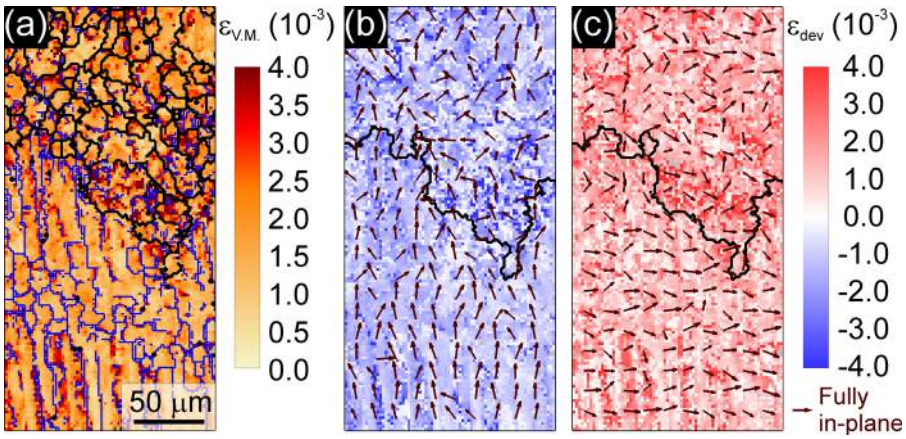

FIG. 4. Distribution maps of (a) von Mises strain, (b) compressive principal strain, and (c) tensile principal strain. In (a) HAGBs and LAGBs are plotted in black and blue, respectively. In (b) and (c), the interface between the dendritic and stray grains is displayed in black, and projections of the principal strain axes on **XY**-plane are denoted by arrows in every 7th pixel. An arrow is plotted at the bottom right corner to define the "fully in-plane" length.

account of the different thermal contraction between dendrite and interdendritic regions as a result of elemental segregation.[7] The cumulative mechanical constraints compel local plastic deformation, resulting in the accumulation of disorientation and defect around the root of the dendrite, where high level of residual strain is frequently preserved.

To evaluate the magnitude of the residual strain, the Von Mises strain $(\varepsilon_{V.M.})$ is calculated and displayed in Figure 4(a). The pixel/angular deviation between the theoretical and experimental peak positions in the Laue pattern after strain refinement is shown in Figure S3 of the supplementary material.[18] High residual strain and large deviation occur in the vicinity of dendrite edges along the LAGBs in blue lines. The magnitude of strain in the dendritic region is slightly lower than that in the stray grain region, so the generation of stray grains is deleterious to the mechanical properties and high-temperature creep resistance of turbine blade. To illustrate the orientation of the deviatoric strain (ε_{dev}) ellipsoid, principal strains and their axes are derived from the eigenvalues and eigenvectors of the strain tensor at each location. Because of the nature of deviatoric strain, the minimum of three eigenvalues is negative, while the maximum is positive, indicating compression and tension, respectively. Given this, we plot the compressive (blue) and tensile (red) principal strain distribution in Figures 4(b) and 4(c), respectively, and delineate a series of arrows in every 7th pixel to denote the direction of principal strain axes projected on the **XY**-plane. The strain axis distribution in stray grain region is found to be inhomogeneous, in association with the random crystal orientation distribution, while the well-aligned arrows reveal uniform distribution of strain tensor orientation in the dendritic region. It is worth noting that the strains shown here are deviatoric, and thus cannot be compared with the full strains reported before,[7] but the relative magnitude is comparable. Vertically aligned compressive strain suggests that the dendrites "contract" along the dendrite growth direction and stretch perpendicular to the primary dendrite axis. However, previous modelling predicts that conventionally solidified Ni-based superalloy stretches in all three dimensions and it is more tensile along the dendrite growth direction than in the transverse direction.[7] We postulate the difference is rooted from the layer-by-layer raster scanning deposition process of 3D printing. With this technique, each freshly deposited layer can be regarded as a free surface, so that the out-of-plane stress, similar to the case in thin films, is close to zero, and thus the strain along the primary dendrite arms is determined by the in-plane stress and has opposite sign to the strain transversely to the dendrite arms. While in the conventional process, solidification occurs continuously and the stress builds up in all three dimensions; therefore, the out-of-plane strain could have the same sign as the in-plane ones. Regarding the origin of the tensile strain perpendicular to the dendrite arms, it is believed to result from the volume shrinkage during the solidification process.

To conclude, the defect inhomogeneity and strain gradient near the transitional region of columnar/cellular dendrites and stray grains in a laser-assisted 3D-printed Ni-based superalloy were probed with synchrotron μXRD technique. The detailed profile of dendrite edges are discerned from the fine crystal orientation deviation, also known as LAGBs, between the dendritic and interdendritic regions. In addition, the LAGBs are the preferential sites for defects (mainly GNDs) and residual strain to build up, which may initiate hot cracks. The interdendritic strain can be attributed to the defects introduced in solidification process and the preservation of thermal stress caused by the contraction misfit between the dendritic and interdendritic regions. Deviatoric strain maps show a relative compression state along the primary dendrite growth direction, and a more tensile state perpendicular to the primary dendrite axes. This is believed to be governed by the local microstructure and thermal contraction controlled by the composition of the superalloy and its processing parameters. Moreover, the strain distribution in stray grain region is much more inhomogeneous owing to the presence of HAGBs.

This work was supported by the National Natural Science Foundation of China (Grant Nos. 51302207, 51275392, and 51271140), the National Basic Research Program of China ("973" Program) (Grant No. 2015CB057400), and the Fundamental Research Funds for the Central Universities (Grant No. 2015gjhz03). K.C. was supported by the National Young 1000 Talents Program of China. The ALS was supported by the Director, Office of Science, Office of Basic Energy Sciences, Materials Science Division, of the U.S. Department of Energy under Contract No. DE-AC02-05CH11231 at LBNL.

[1]T. M. Pollock and S. Tin, J. Propul. Power **22**, 361 (2006).
[2]R. Vilar and A. Almeida, J. Laser Appl. **27**, S17004 (2015).

[3]S. Mokadem, C. Bezençon, A. Hauert, A. Jacot, and W. Kurz, Metall. Mater. Trans. A **38**, 1500 (2007).
[4]M. Gäumann, S. Henry, F. Cléton, J.-D. Wagnière, and W. Kurz, Mater. Sci. Eng., A **271**, 232 (1999).
[5]Y. Amouyal, Z. Mao, C. Booth-Morrison, and D. N. Seidman, Appl. Phys. Lett. **94**, 041917 (2009).
[6]Y. Tu, Z. Mao, and D. N. Seidman, Appl. Phys. Lett. **101**, 121910 (2012).
[7]A. Epishin, T. Link, U. Brückner, B. Fedelich, and P. Portella, in *Proceedings of the Tenth International Symposium on Superalloys* (Seven Springs, PA, 2004), pp. 537–543.
[8]L. Felberbaum, K. Voisey, M. Gäumann, B. Viguier, and A. Mortensen, Mater. Sci. Eng., A **299**, 152 (2001).
[9]X. Do, D. Li, A. Zhang, B. He, H. Zhang, and T. Doan, J. Laser Appl. **25**, 012007 (2013).
[10]M. Kunz, N. Tamura, K. Chen, A. A. MacDowell, R. S. Celestre, M. M. Church, S. Fakra, E. E. Domning, J. M. Glossinger, J. L. Kirschman, G. Y. Morrison, D. W. Plate, B. V. Smith, T. Warwick, V. V. Yashchuk, H. A. Padmore, and E. Ustundag, Rev. Sci. Instrum. **80**, 035108 (2009).
[11]N. Tamura, in *Strain Dislocation Gradients from Diffraction. Spatially-Resolved Local Structure and Defects*, edited by R. Barabash and G. Ice (World Scientific, London, 2014), pp. 125–155.
[12]K. Chen, N. Tamura, W. Tang, M. Kunz, Y. C. Chou, K. N. Tu, and Y. S. Lai, J. Appl. Phys. **107**, 063502 (2010).
[13]K. Chen, M. Kunz, N. Tamura, and H.-R. Wenk, Geology **43**, 219 (2015).
[14]A. Lupinacci, K. Chen, Y. Li, M. Kunz, Z. Jiao, G. S. Was, M. D. Abad, A. M. Minor, and P. Hosemann, J. Nucl. Mater. **458**, 70 (2015).
[15]K. Chen, N. Tamura, B. C. Valek, and K. N. Tu, J. Appl. Phys. **104**, 13513 (2008).
[16]Y. Li, L. Wan, and K. Chen, J. Appl. Crystallogr. **48**, 747 (2015).
[17]N. Siredey, M. Boufoussi, S. Denis, and J. Lacaze, J. Cryst. Growth **130**, 132 (1993).
[18]See supplementary material at http://dx.doi.org/10.1063/1.4934839 for the distributions of crystal orientation of the substrate, Euler angles and rotation axes, peak position deviation, and residual strain in the substrate in Figures S1, S2, S3, and S4, respectively.
[19]B. C. Valek, N. Tamura, R. Spolenak, W. A. Caldwell, A. A. MacDowell, R. S. Celestre, H. A. Padmore, J. C. Bravman, B. W. Batterman, W. D. Nix, and J. R. Patel, J. Appl. Phys. **94**, 3757 (2003).
[20]N. S. Husseini, D. P. Kumah, J. Z. Yi, C. J. Torbet, D. A. Arms, E. M. Dufresne, T. M. Pollock, J. Wayne Jones, and R. Clarke, Acta Mater. **56**, 4715 (2008).
[21]J. W. Aveson, P. A. Tennant, B. J. Foss, B. A. Shollock, H. J. Stone, and N. D'Souza, Acta Mater. **61**, 5162 (2013).
[22]J. Xue, A. Zhang, Y. Li, D. Qian, J. Wan, B. Qi, N. Tamura, Z. Song, and K. Chen, Sci. Rep. **5**, 14903 (2015).